Effect of minor addition of Zn on precipitate crystal structures and intergranular corrosion in 6082 Al-Mg-Si alloys

Bartawi, Emad H.; Shaban, Ghada; Marioara, Calin D.; Rahimi, Ehsan; Bjørge, Ruben; Sunde, Jonas K.; Gonzalez-Garcia, Yaiza; Holmestad, Randi; Ambat, Rajan

DOI
10.1016/j.corsci.2025.112844

Publication date
2025

Document Version
Final published version

Published in
Corrosion Science

Citation (APA)
Bartawi, E. H., Shaban, G., Marioara, C. D., Rahimi, E., Bjørge, R., Sunde, J. K., Gonzalez-Garcia, Y., Holmestad, R., & Ambat, R. (2025). Effect of minor addition of Zn on precipitate crystal structures and intergranular corrosion in 6082 Al-Mg-Si alloys. *Corrosion Science*, *249*, Article 112844. https://doi.org/10.1016/j.corsci.2025.112844

Corrosion Science 249 (2025) 112844

Contents lists available at ScienceDirect

Corrosion Science

journal homepage: www.elsevier.com/locate/corsci

Effect of minor addition of Zn on precipitate crystal structures and intergranular corrosion in 6082 Al-Mg-Si alloys

Emad H. Bartawi [a,*], Ghada Shaban [a], Calin D. Marioara [b], Ehsan Rahimi [c], Ruben Bjørge [b], Jonas K. Sunde [d], Yaiza Gonzalez-Garcia [c], Randi Holmestad [e], Rajan Ambat [a]

[a] Section of Materials and Surface Engineering, Department of Civil and Mechanical Engineering, Technical University of Denmark, Kongens Lyngby 2800, Denmark
[b] Materials and Nanotechnology, SINTEF Industry, Trondheim N-7465, Norway
[c] Department of Materials Science and Engineering, Delft University of Technology, Mekelweg 2, Delft 2628 CD, the Netherlands
[d] Hydro, Innovation & Technology, Drammensveien 264, Oslo 0283, Norway
[e] Department of Physics, NTNU, Norwegian University of Science and Technology, Trondheim 7491, Norway

ARTICLE INFO

Keywords:
Al-Mg-Si alloy
Intergranular corrosion
Precipitate crystal structure
HAADF-STEM
SKPFM

ABSTRACT

Recycling Al alloys promotes greater sustainability, as the energy required to produce recycled alloys is only about 5 % of that needed to produce the same amount of primary alloys. However, the build-up of impurities, such as Zn, during the recycling process can negatively affect the corrosion resistance of recycled alloys. The results show that the susceptibility to intergranular corrosion increased with minor additions of zinc ($\leq$ 0.06 wt %). Zn was found to segregate along the grain boundaries, and the STEM-EDS results indicate that the Zn incorporates into the structure of Mg-Si containing grain boundary precipitates.

1. Introduction

Weight reduction in automotive applications is an effective strategy to reduce energy consumption and, thus, CO_2 emissions [1]. Consequently, it comes as no surprise that heat treatable Al-Mg-Si alloys showed considerable potential in future automotive applications owing to their many attractive properties, such as low density, good formability, recyclability, high strength-to-weight ratio, and outstanding corrosion resistance [2–5]. However, other challenges remain to be considered, such as improving paint baking response, formability, and localized corrosion resistance [6–9]. Although Al-Mg-Si alloys generally demonstrate acceptable corrosion resistance, intergranular corrosion (IGC) can sometimes be notable due to the presence of certain alloying elements (e.g., Cu and Zn additions) or lack of control in thermal processing (e.g. slow quenching after extrusion). It is believed that intergranular corrosion in Al-Mg-Si alloys takes place as a result of microgalvanic coupling between grain boundary particles acting as anodes and the solute depleted precipitate free zone (PFZ) acting as cathode [10–14]. Shi et al. [12] studied the localized corrosion resistance of a Cu-free Al-0.61Mg-0.76Si (wt%) alloy. It was claimed that IGC in such alloys occurs due to Si segregation to the grain boundaries (GBs) acting as an effective cathode promoting IGC. The same observation was made by Bhattamishra and Lal [15], who explored Al-0.4Mg-1.0Si alloy.

It is also claimed that the Mg/Si ratio considerably affects the IGC resistance of Al-Mg-Si and Al-Mg-Si-Cu alloys [10,11]. Kairy et al. [10] argued that Cu-free Al-Mg-Si alloys with a lower Mg/Si ratio (0.336) were more susceptible to IGC than alloys with a higher Mg/Si ratio (2.192) in the peakaged (PA) condition. It is generally accepted that Cu additions at notable concentrations (approx. $\geq$ 0.1 wt%) can negatively influence the IGC resistance of Al-Mg-Si alloys in the underaged (UA) and PA conditions. The IGC in Al-Mg-Si-Cu alloys is attributed to microgalvanic coupling between grain boundary particles, Cu-rich films located along GBs, and precipitate-free zones [16–22]. According to Zou et al. [11], Cu-containing alloys with a lower Mg/Si ratio (0.55) exhibited a severe IGC, while alloys with a higher Mg/Si ratio (2.13) showed improved corrosion resistance as pitting corrosion was the primarily observed corrosion mechanism.

To date, the literature lacks studies investigating the influence of minor Zn concentrations ($\leq$ 0.06 wt%), anticipated to be found in recycled Al-Mg-Si alloys, focusing on their effect on alloy microstructure and IGC resistance. It was reported that relatively high Zn ($\geq$ 0.5 wt%) additions can significantly influence the precipitation and improve age hardening response in Al-Mg-Si alloys due to an increased volume fraction of clusters compared to Zn-free alloys [23–28]. The results of

* Corresponding author.
E-mail address: ehaba@dtu.dk (E.H. Bartawi).

https://doi.org/10.1016/j.corsci.2025.112844
Received 4 October 2024; Received in revised form 1 March 2025; Accepted 1 March 2025
Available online 12 March 2025

Saito et al. [29] showed that Zn-added Al-0.5Mg-0.4Si alloys ($\leq$ 1 wt%) achieved a modest increase in hardness as a function of Zn content, which is related to the rise in the number density of needle-shaped precipitates. Moreover, no precipitates of the Al-Mg-Zn (Mg-Zn η-type) alloy system were detected in their studied alloys. Zhu et al. [30] also found that a 0.6 wt% Zn addition did not alter the precipitation sequence of an artificially aged Al-0.9Mg-0.8Si alloy. At the same time, the improvement in the age hardening response and thus the mechanical properties observed in a Zn-added alloy ($\geq$ 2.37 wt%) are attributed to the formation of η-$MgZn_2$ phase precipitates and its precursor normally found in the Al-Mg-Zn system [28,31].

On the topic of IGC, Saito et al. [29] investigated the influence of Zn ($\leq$ 1 wt%) on the IGC resistance of Al-Mg-Si in T6 temper. The results showed that alloys with Zn addition $\leq$ 0.11 wt% exhibited negligible IGC susceptibility. However, severe IGC was recorded in the alloy containing 1 wt% Zn, indicating that there is a critical level of Zn additions affecting the IGC resistance of Al-Mg-Si alloy is set between 0.11 and 1 wt%. It is also reported that Zn diffuses into precipitates when Zn content is 1 wt%, while the distribution of Zn is not described when Zn concentration is $\leq$ 0.11 wt% [29]. Therefore, understanding the influence of low Zn additions on Al-Mg-Si alloys, as a result of recycling, on the microstructure and IGC is the key focus of this work.

It appears that Zn concentrations between 0.003 and 0.06 wt% are critical to defining the IGC resistance of recycled Al-Mg-Si alloys. Moreover, the influence of small concentrations of Zn on Al-Mg-Si precipitate crystal structures is still not understood. Therefore, the present study aims to elucidate how trace levels of Zn affect the microstructure and IGC resistance of Al-Mg-Si alloys, focusing on the industrially important 6082 Al-Mg-Si alloy. The microstructure was investigated using optical microscopy. Scanning electron microscopy (SEM) analysis was conducted on the surface and cross-section of the corroded samples to examine the extent and the penetration depth, respectively. Scanning transmission electron microscopy (STEM) was used to study microstructure and grain boundary chemistry. Atomic resolution STEM was utilized to analyze the influence of 0.06 wt% Zn on the precipitate structures. Furthermore, atomic force microscopy (AFM) coupled with scanning Kelvin probe force microscope (SKPFM) was employed to measure the surface potential difference along the grain boundary to elucidate the role of Zn.

2. Experimental methods

2.1. Material used

The extruded Al-Mg-Si alloys with different minor additions of Zn were manufactured to imitate the expected Zn level in recycled Al-Mg-Si alloys. The cast ingots were homogenized at 575 °C for 135 min according to industrial practice. Thereafter, the material was hot extruded at a ram speed of 5.6 mm/s and at an average temperature of 530 °C into flat profiles and water-quenched. Subsequently, the material profiles were stretched 0.5 %, underwent two-step aging to reach the PA condition. Hydro Aluminium identified the achieved temper as T6.

Four alloy specimens with different Zn content (0.003, 0.02, 0.04, and 0.06 wt%) were labeled R1, R2, R3, and R4, respectively (see Table 1).

Table 1
Chemical composition (wt%) of the artificially aged 6082 Al-Mg-Si alloy used in the present study.

Alloy	Al	Mg	Si	Zn	Cu	Fe	Mn
R1	Balance	0.65	0.97	0.003	0.001	0.22	0.54
R2	Balance	0.64	0.96	0.022	0.001	0.21	0.55
R3	Balance	0.64	0.94	0.041	0.001	0.21	0.54
R4	Balance	0.63	0.94	0.059	0.001	0.21	0.56

2.2. Microstructure characterization

Microstructure was first characterized using a Zeiss Axio Vert.A1 light optical microscope. Three main directions of observation are used in the following, referred to as extrusion direction (ED), transverse direction (TD), and normal direction (ND), which can be seen in Fig. 1. The 3D microstructure imaging of the samples is obtained from samples of 25 × 10 x 4 mm^3 size. The samples were ground, mechanically polished to 1 μm, and then electrochemical etched in tetrafluoroboric acid for 60 s before the analyses [14]. After a 24 h immersion test, the corrosion morphology of the cross-section and surface was studied using an AFEG 250 Analytical ESEM operated under a high-vacuum atmosphere.

Transmission electron microscope (TEM) specimens were prepared from the top surface of the recrystallized layer of the extruded material profiles, see Fig. 1. The samples were firstly mechanically thinned by polishing to a thickness of approximately 100 μm and then punched into 3 mm diameter thin foils. The foil disks were then electropolished at — 25°C in a Struers A2 solution using a TenuPol-5 twin-jet system. Two TEM instruments were used in this work. (i) A spherical aberration (Cs) probe-corrected Titan Analytical 80–300ST microscope was employed to investigate the microstructure and grain boundary chemistry. The microscope was operated at 300 kV along with a windowless X-Max 80TLE detector. (ii) A spherical aberration (Cs) probe-corrected JEOL ARM200CF was used to acquire atomically resolved high-angle annular dark-field (HAADF) STEM images operated at 200 kV using a detector collection angle of 42–178 mrad.

2.3. AFM and SKPFM surface characterization

To investigate the impact of Zn on the surface potential near alloy grain boundaries, atomic force microscopy (AFM) coupled with scanning Kelvin probe force microscopy (SKPFM) analysis was conducted. The samples were prepared by polishing to 0.25 μm followed by 30 s of OP-S and then samples were cleaned with distilled water, rinsed with ethanol, and thoroughly dried. The GBs of interest were then marked by a combined focused ion beam and scanning electron microscope (FIB-SEM). Following FIB preparation, the samples were stored in a desiccator for one week before performing AFM/SKPFM measurements.

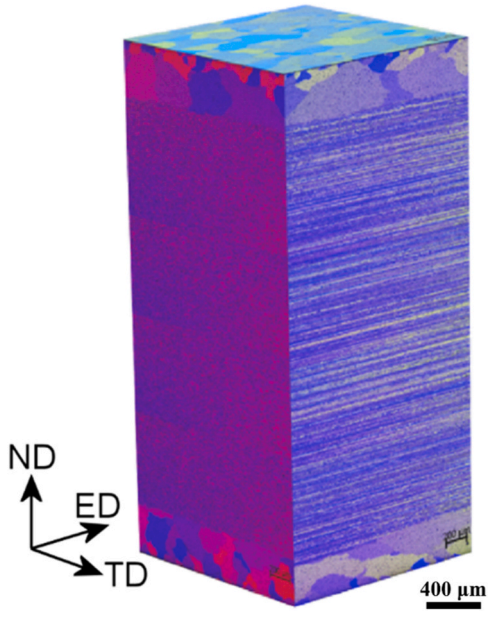

Fig. 1. 3D-optical observation illustrating the grain structure of the extruded 6082 (R1) in the PA condition after electrochemical etching in tetrafluoroboric acid.

AFM/SKPFM measurements were performed by a Bruker Dimension Edge™ instrument with an n-type doped silicon pyramid single crystal tip coated with PtIr5 (SCM-Pit probe), with a height and tip radius of 10–15 μm and 20 nm, respectively. The local electronic surface potential was recorded in dual-scan mode. In the first scan, the topography map was recorded in tapping mode. The tip was lifted to 100 nm in the second scan, and the surface potential was obtained by following the topography registered in the first scan. Both the topography and surface potential images were captured under ex-situ conditions in an approximate relative humidity of 32 % and at 22 °C. Moreover, the following parameters were fixed for all AFM/SKPFM tests: pixel resolution of 512 × 512, tip-biased, zero-DC bias voltage, and scan frequency rate of 0.3 Hz.

2.4. IGC test

Corrosion tests were conducted on samples with a size of 25 × 20 x 4 mm^3 by immersion in an acidified salt solution for 24 h according to BS-ISO 11846 method B. The samples were degreased in action, etched in 8 wt% sodium hydroxide solution for 5 min at 55 °C, rinsed in distilled water, and then desmutted in concentrated nitric acid. Before the IGC tests, the narrow sides of all tested specimens were lacquered by Lacomit varnish to avoid possible interference between the deformed and the recrystallized layers, as the former is more active than the latter. The IGC test was conducted by immersing the samples in acidified salt solution containing 10 ml/l HCl and 30 g/l NaCl. After 24 h immersion, the samples were thoroughly washed in distilled water, ethanol and then air-dried. Thereafter, the surface and cross-section morphologies were investigated using SEM.

3. Results

3.1. Microstructure characterization

All investigated samples revealed a dual microstructure comprising a recrystallized surface layer of approximately 400 μm thickness and a deformed center layer, as illustrated in Fig. 1 for sample R1. Although not shown, all other alloys showed similar microstructural features as for sample R1 shown in Fig. 1. It is worth noting that the grain sizes of the recrystallized surface layer vary with depth. The average size of the grains on the top surface is around 30 μm, while the grain size near the deformed layer can be several hundred micrometers, as also observed in our previous work [14]. In the present research work, attention was given to exploring the recrystallized layer.

3.2. Intergranular corrosion susceptibility of the studied samples

Fig. 2(a-d) shows the alloy surfaces after 24 h immersion in an acidified salt solution, revealing a noticeable difference in the IGC attack for different alloys. A typical localized IGC corrosion is observed in samples R1 and R2, whereas a transition toward a more uniform IGC is observed in sample R3, and a heavy uniform IGC is recorded in sample R4. A noticeably higher number of attacked grain boundaries is observed in sample R2 compared to sample R1, indicating that sample R1 has a higher IGC resistance than sample R2.

Fig. 3(a-d) shows the cross-sectional IGC morphology of the studied alloys in PA condition after 24 h immersion in an acidified salt solution. The maximum observed penetration depth of 137 μm is found in sample R4 with the highest Zn addition. Observations of IGC extension and penetration with respect to Zn additions indicate that minor Zn

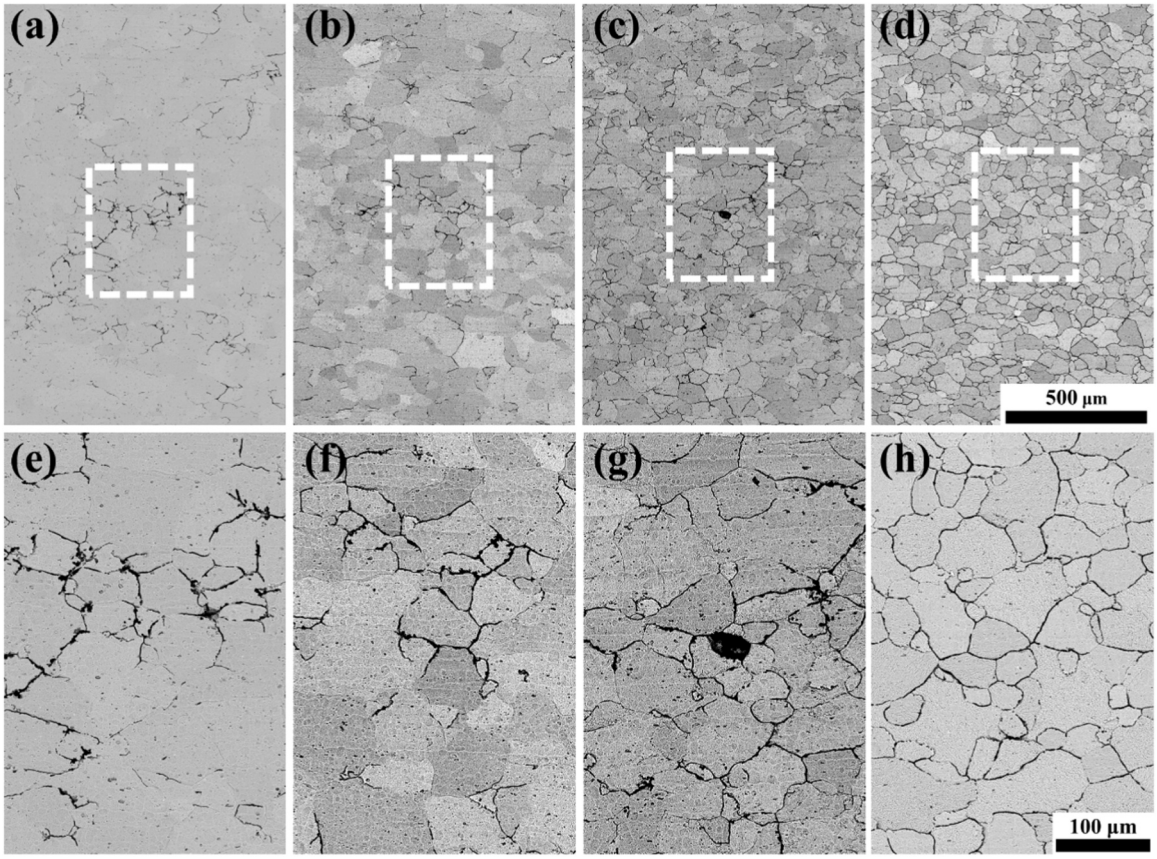

Fig. 2. SEM-BSE micrographs of the surface morphology after 24 h immersion in acidified salt solution of: (a) alloy R1, (b) alloy R2, (c) alloy R3, and (d) alloy R4. The corresponding regions for each alloy marked by dotted line rectangles are shown magnified in (e) to (h). The scale bar in (d) applies to (a)-(c), and the scale bar of (h) applies to (e)-(g).

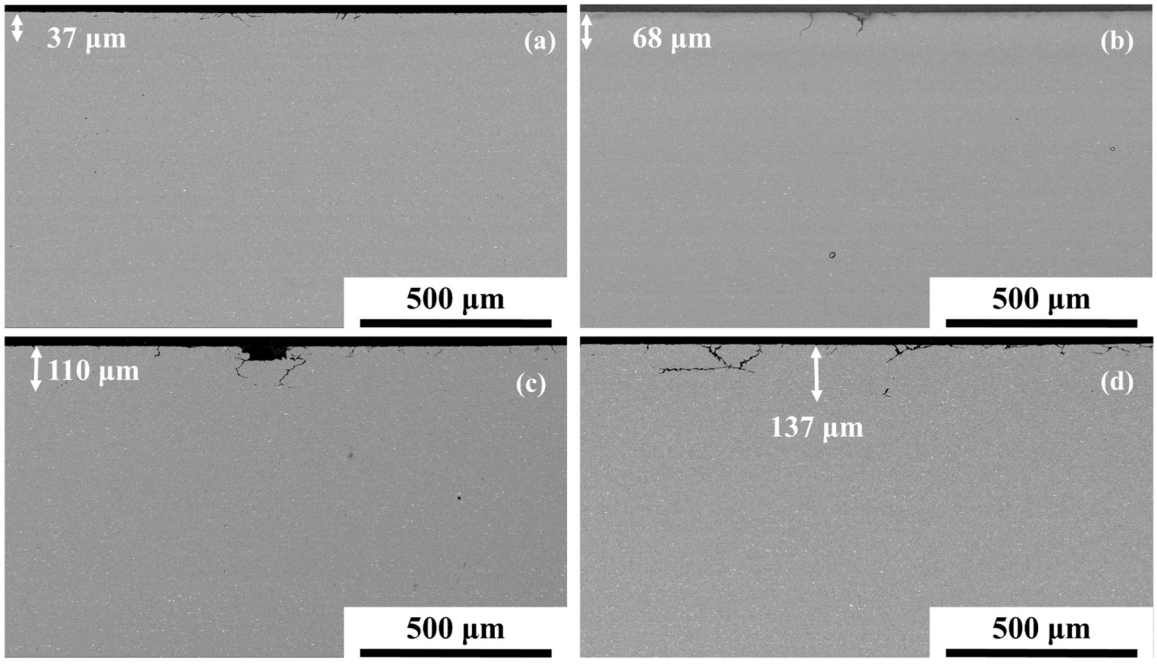

Fig. 3. SEM-BSE micrographs of the cross-section morphology after 24 h immersion in acidified salt solution of: (a) alloy R1, (b) alloy R2, (c) alloy R3, and (d) alloy R4.

additions have a stronger influence on the lateral IGC attack than on the penetration depth, as the latter only shows a slight increase with Zn concentration, as illustrated in Fig. 3.

Observations of IGC extension and penetration with respect to the Zn additions indicate that minor Zn additions have a higher negative influence on the IGC attack laterally than the penetration depth, as the latter only slightly increased as a function of Zn concentrations, see Fig. 3.

3.3. (S)TEM analysis of grain boundaries and precipitates

The bright field-TEM images of the four examined alloys with the

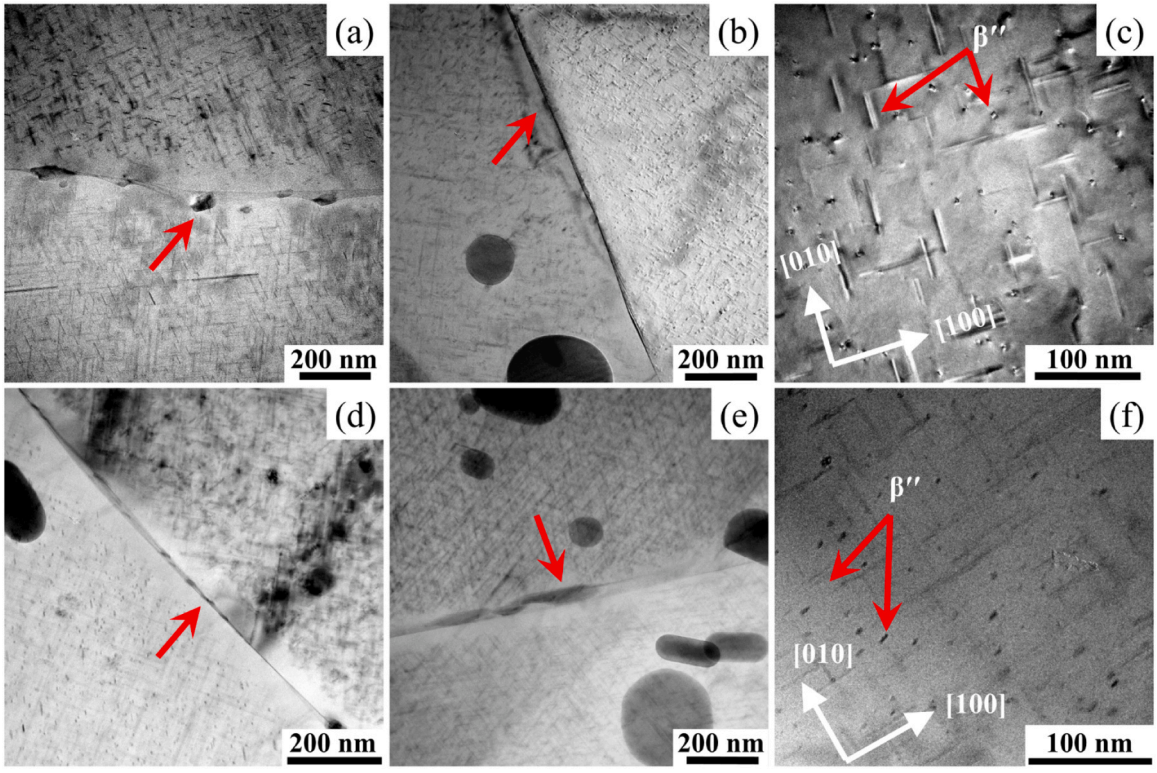

Fig. 4. Typical TEM images of Al-Mg-Si alloy in the PA condition; (a) alloy R1, (b) alloy R2, (c) alloy R1 microstructure observed in < 100 > Al zone axis, (d) alloy R3, (e) alloy R4, and (f) alloy R4 microstructure observed in < 100 > Al zone axis. Red arrows in (a), (b), (d) and (e) indicate grain boundary precipitates, while in (c) and (f) indicate hardening precipitates.

grain boundaries orientated parallel to the incident electron beam are shown in Fig. 4. Precipitate free zones (PFZ) of approximately 100 nm width can be readily observed along the grain boundaries of all investigated alloys. Moreover, observation of several grain boundaries for all studied alloys confirmed the presence of particles located along the grain boundaries. The density of such precipitates varied from grain boundary to grain boundary. However, some investigated grain boundaries of sample R1 are free from particles. Dispersoids and intermetallic particles are detected in the microstructure of the studied alloys. Such particles showed dark contrast as they contain heavy elements (Mn and Fe), which scatter electrons more intensely than the adjacent aluminium matrix. The precipitates in the grain interior are moderately different in samples R1 and R4, see Fig. 4(c, f), as slightly denser and finer precipitates are observed in sample R4 compared to sample R1.

To analyze the influence of minor additions of Zn on grain boundary chemistry, EDS-STEM (HAADF) analysis was performed on samples R1 and R4. The results obtained from sample R1 revealed grain boundaries free of particles as well as grain boundaries containing particles enriched in Si and Mg, identified as Mg-Si precipitates, see Fig. 5. The EDS maps also reveal the presence of Mg and Si depleted zone of approximately 100 nm in the vicinity of the grain boundary, see Fig. 5d. Moreover, no clear Zn-containing particles or Zn-rich films are detected at such low Zn concentration, see Fig. 5(b, d).

Fig. 6 displays two typical grain boundaries of the sample R4, revealing the presence of grain boundary particles. Fig. 6b shows relatively distantly separated GB particles, while in Fig. 6d, the GB particles are closely spaced, forming a Zn path. The corresponding EDS elemental maps in Fig. 6(b, d) reveal that such precipitates are rich in Mg, Si, and with clear presence of Zn. Interestingly, noticeable Mg and Si depletion along the grain boundary can be noticed, but not for Zn. Moreover, no distinct continuous film rich in Zn is detected along the grain boundary. This indicates that Zn is more uniformly distributed in the PFZ and grain interior.

Atomic resolution Z-contrast HAADF-STEM imaging was conducted on sample R4 to explore whether 0.06 wt% Zn will influence the crystal structure of hardening precipitates observed in its microstructure and demonstrated in Fig. 7. The hardening precipitates of Al-Mg-Si alloys grow in⟨0 0 1⟩Al directions. Therefore, all images were taken at⟨0 0 1⟩Al zone axis orientation. To minimize the noise, fast Fourier transform (FFT) filtering is applied through a circular band pass mask to remove all distances shorter than 1.5 Å. Atomic overlay was conducted on representative β″ precipitates based on the construction rules of precipitates in the Al-Mg-Si(-Cu) alloy system from [32], atomic number Z-contrast and on similarity to well-known precipitate crystal structures in Al-Mg-Si alloys [33–35]. Fig. 7a shows FFT-filtered images of a β″ precipitate found in the bulk of sample R4. The atomic overlay shows that the precipitate consists of eye structural configurations. Interestingly, Zn is observed to occupy Si_1, Si_2, and Si_3/Al in the β″ structural unit. Furthermore, Zn is noticed to partially occupy Si_1 columns in β″

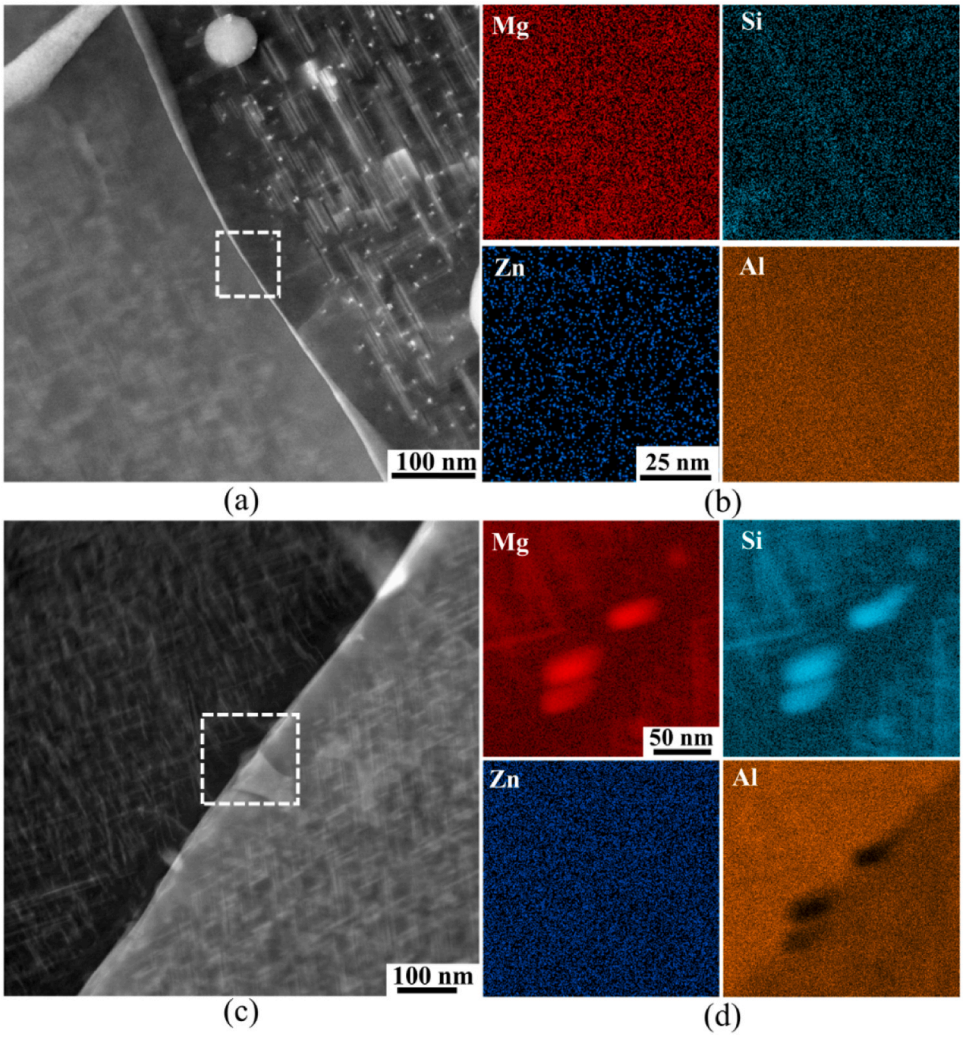

Fig. 5. HAADF-STEM images showing two grain boundaries for alloy R1 in the PA condition, containing 0.003 wt% Zn and their corresponding Al, Mg, Si, and Zn EDS elemental maps at the grain boundaries regions.

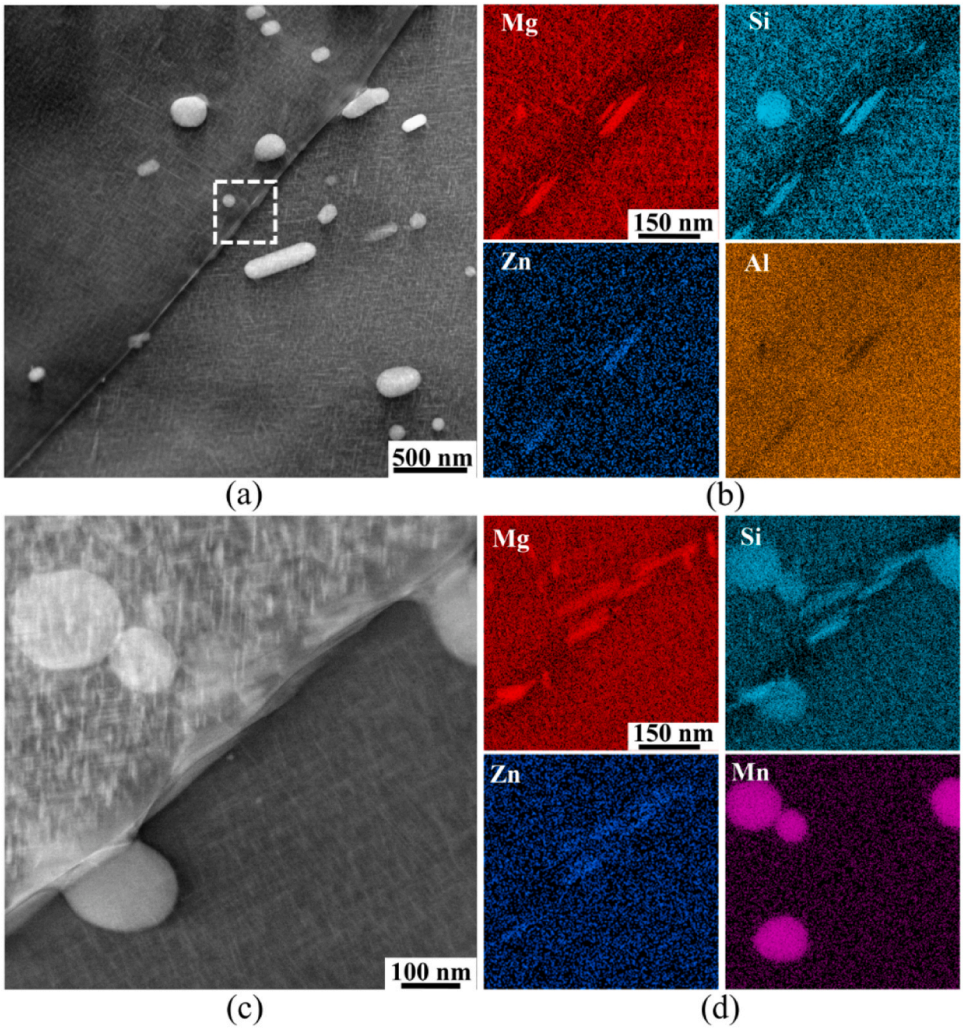

Fig. 6. HAADF-STEM images showing two grain boundaries for sample R4 alloy in the PA condition, containing 0.06 wt% Zn and their corresponding Al, Mg, Si, and Zn EDS elemental maps of the grain boundary regions.

precipitates/Al interface, see Fig. 7c. Also, a Q′/C local configuration is observed in the β″ structure, see Fig. 7d.

3.4. AFM/SKPFM analysis of grain boundaries

The presence of Zn-enriched precipitates located along the grain boundaries of sample R4 which was not evident in sample R1 (lowest amount of Zn) leads to a difference in the chemical behavior and especially electronic properties at grain boundary. The electronic properties probed here include surface charge, electrical surface potential or work function (∅). Therefore, revealing some information related to these electronic properties' evolutions at the GB with and without Zn-enriched precipitates can give better knowledge to predict the different driving forces for galvanic coupling at the GB (e.g. intergranular corrosion attacks) [36]. On this account, AFM coupled with SKPFM maps of grain boundaries in two different alloys namely R1 without Zn and R4 with Zn-enriched particles were conducted to evaluate the electrical surface potential and/or surface charge difference at the GB. The SEM image in Fig. 8(a) shows the presence of triple boundary points. Fig. 8(c, d) presents topography and surface potential maps of grain boundaries at a triple junction in sample R1. Three intermetallic particles (IMPs) are also located in the scanned region, one of which is located on or close to a GB. From the surface potential map and its corresponding histogram analysis (Fig. 8e), it is observed that the IMPs have the lowest and different surface potential compared to the Al matrix. The surface potential difference between IMPs and Al matrix is in the range of ~40–70 mV.

Utilizing the line profile of topography and its corresponding surface potential across three different grain boundaries, Fig. 8(f, g, h), it was noticed that all grain boundaries approximately exhibit the same surface potential difference value (~4 or 5 mV) compared to the grain boundary adjacent (~200 nm). However, in the case of sample R4, AFM and SKPFM maps exhibit a better recognizable grain boundary with a higher surface potential distribution (brighter color) than the Al matrix, as presented in Fig. 9(d). In addition, the two-line profiles of topography and corresponding surface potential in Fig. 9(e, f) indicate that the grain boundary region in sample R4 has a higher surface potential difference (~10 mV) than sample R1 (~4 mV). It is important to specify that since the tip is biased the low potential (dark region) indicates the cathode and the higher potential (bright region) indicates the anode [37].

4. Discussion

The focus of the present study was to investigate the effect of very low levels of Zn on IGC of surface layer of the extruded material, characterized by peripheral coarse grains (PCG). Such coarse-grained surface layers can be found in medium to high-strength 6082 Al-Mg-Si alloys used in many industrial applications, including the automotive sector. It is reported that the formation and extension of the PCG layer are closely linked to alloy composition, homogenization temperature, extrusion

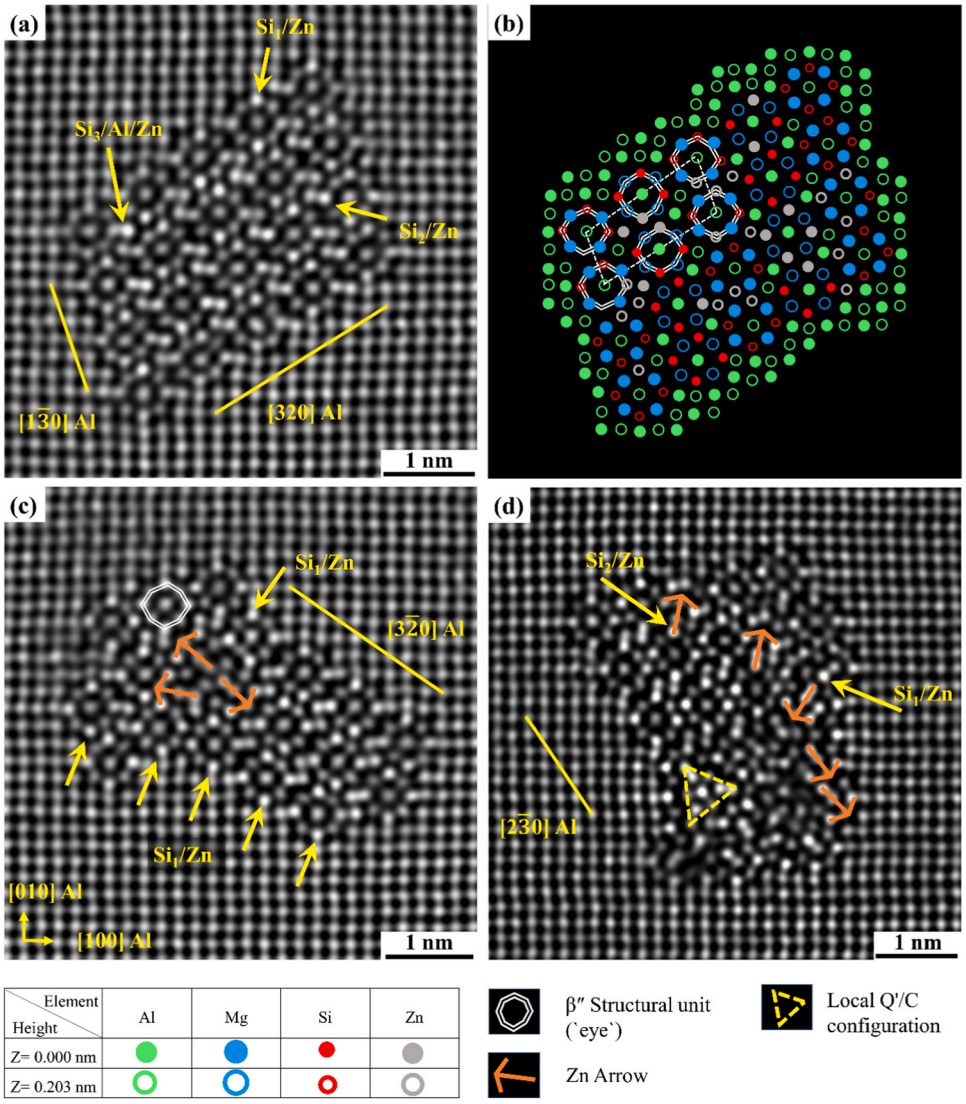

Fig. 7. (a, c, and d) HAADF-STEM image of Zn containing β'' precipitates cross-section taken from alloy R4 with 0.06 Zn wt%. (a) FFT Filtered image, (b) suggested overlay of (a) based on the construction rules and Z-contrast (Al, Mg, Si, and Zn are considered).

parameters, and die design [38–40]. The primary motivation of this work is to examine the influence of the minor addition of Zn ≤ 0.06 wt% expected to be found in recycled Al-Mg-Si alloys on the IGC resistance of the recrystallized surface layer, and how Zn affects the age hardening precipitates formed.

4.1. Microstructure investigation

The morphology of the bulk precipitates in samples R1 and R4 shown in Fig. 4(c, f) and the atomic structures in Fig. 7 indicate that the vast majority of these precipitates are β″ (needle-shaped) with a minor fraction of β′ (rod-shaped) precipitates. Slightly finer and denser precipitates can be observed in sample R4 compared with sample R1. Ding et al. [28] have investigated the influence of 0.5 and 3 wt% Zn on the age hardening response of Al-0.98Mg-0.44Si and Al-0.99Mg-0.54Si alloys at different aging conditions. The results showed that the meta-stable precursor phases of β-Mg_2Si precipitates (β″) are the main phase when the Zn concentration is 0.5 wt%. However, the meta-stable precipitates of η-$MgZn_2$ can be formed in the microstructure of 3 wt% Zn-containing Al-Mg-Si in the PA condition. In the current work, no Mg-Zn precipitates were observed in the microstructure of sample R4 as such a minor addition of Zn did not change the precipitation sequence of studied 6082 Al-Mg-Si alloys. However, 0.06 wt% Zn noticeably enters the composition of primary hardening precipitates (β″) observed in the current study, as seen from Fig. 7(c, d).

Saito et al. [29] studied the influence of different levels of Zn on mechanical and corrosion properties, as well as on precipitate structures in an Al-0.5Mg-0.4Si model alloy. The results showed that the alloy with 1.02 wt% Zn addition produced disordered precipitates in PA condition as a low amount of Zn entered the precipitate crystal structures. At the same time, it is concluded that alloys with Zn ≤ 0.1 wt% did not show a measurable influence on the precipitate structures, mechanical properties and IGC susceptibility as defined by corrosion depth. Interestingly, our investigations of sample R4 show that, although Zn does not affect precipitate structures, it incorporates into various sites (atomic columns) of β″ phase, with affinity to partly replace Si_1, Si_2, and Si_3/Al, see Fig. 7(a, c, d).

4.2. Effect of Zn on intergranular corrosion

The findings from the current research reveal that low levels of Zn can clearly affect the IGC resistance and precipitate structures of the PA 6082 Al-Mg-Si alloys. As shown in Fig. 2, considerable differences between the four studied alloys in susceptibility to IGC can be observed. In

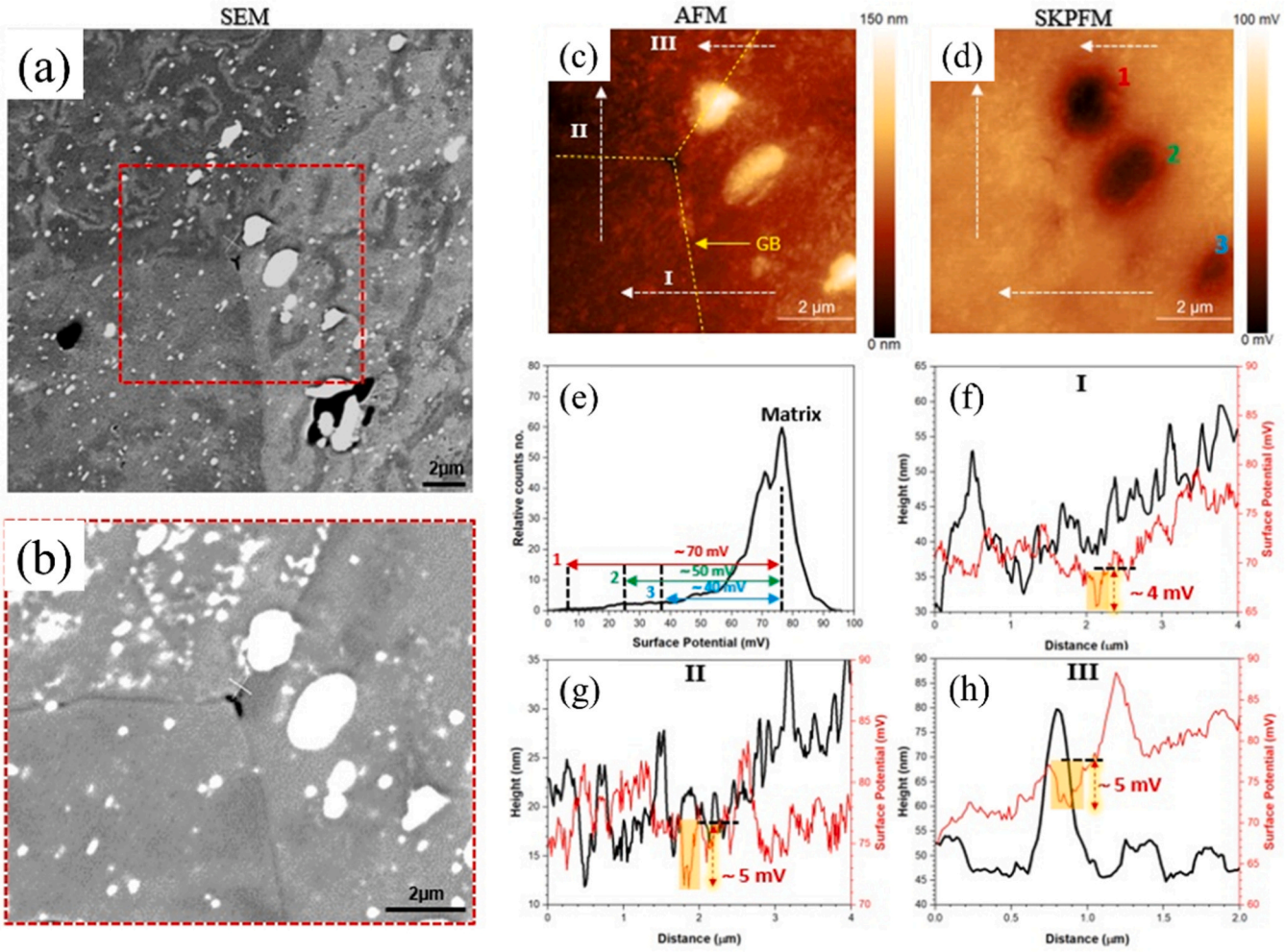

Fig. 8. (a) Low and (b) high magnification SEM images of triple grain boundary point. (c) topography and (d) surface potential maps of alloy R1 near triple grain boundary point. (e) Surface potential histogram of SKPFM map in (d) that visualizes the surface potential difference between three distributed intermetallic particles and the Al matrix. (f, g, and h) Topography and surface potential line profiles in (c) and (d).

sample R4, IGC nearly invaded the surface as a uniform IGC, while less severity was recorded in samples R3, R2, and R1, respectively. The IGC in sample R1 can be explained by the selective anodic dissolution of β (Mg_2Si) precipitates located along the GBs as a result of microgalvanic coupling with the PFZ acting as a cathode [10,12,41]. In addition, the presence of a trace level of Cu in this alloy might also play a role as a discontinued Cu-rich film was reported by Bartawi et al. [13,42]. The susceptibility to IGC increased by increasing the Zn addition indicating that the deterioration observed in the IGC resistance is directly attributed to the minor addition of Zn.

Saito et al. [29] showed that alloys with 0.002, 0.012, and 0.11 wt% Zn (Al-0.5Mg-0.4Si) had negligible IGC susceptibility. Therefore, the authors concluded that Zn content below 0.1 wt% has limited impact on the IGC resistance in Al-Mg-Si alloys. The EDS-STEM investigations of several grain boundaries for sample R4 did not show a distinguished Zn-depleted zone, see Fig. 6. This observation is supported by the experimental work conducted by Saito et al. [29], as no distinguished Zn-depleted zone was recorded. Therefore, it can be concluded that the global solute concentration of Zn in the depleted zone is slightly different from their concentrations in the matrix as HR-STEM conducted on the precipitates in the grain interior confirmed that these precipitates consume the Zn. This implies that the corrosion potential of the depleted zone will be slightly different than the corrosion potential of the matrix. Consequently, the driving force for IGC recorded in sample R4 was due to the microgalvanic coupling between the PFZ as a cathode, and the Zn-rich precipitates decorating the GBs serving as an anode and at the same time, the adjacent Al matrix will act as a cathode leading to the dissolution of the PFZ. This observation is supported by the SKPFM results, as a lower potential was measured at the GB region at the width of approximately 200 nm to reach its peak value at the width of approximately 100 nm, see Fig. 9. Therefore, it can be stated that the average potential of the near grain boundary (Al matrix) is slightly higher (acting as a cathode) than the grain boundary region (acting as an anode). It is essential to mention that the formation of a native oxide film, specifically in the aluminum alloy (γ-Al_2O_3 with a large band gap energy) [43], significantly affects the total surface potential and/or surface charge distribution. This will lead to less tendency to establish an intensive electrostatic force between metal/oxide and tip-apex in SKPFM surface-sensitive technique [44]. The more pronounced signal in sample R4, compared to sample R1, is attributed to the presence of Zn in the grain boundary particles, which shifts the surface potential of the GBs to more negative values. This shift suggests that the grain boundaries will have a lower corrosion potential than the adjacent matrix, implying that the adjacent matrix will act as a cathode relative to the PFZ and GBs. Moreover, The IMPs observed in TEM images (e.g., Fig. 6) show different surface potential with respect to the adjacent region. The various observed values with respect to the Al matrix are due to the variation in the chemical composition and different oxide films on top of them compared to the Al matrix.

A schematic representation of the fundamental principle of SKPFM

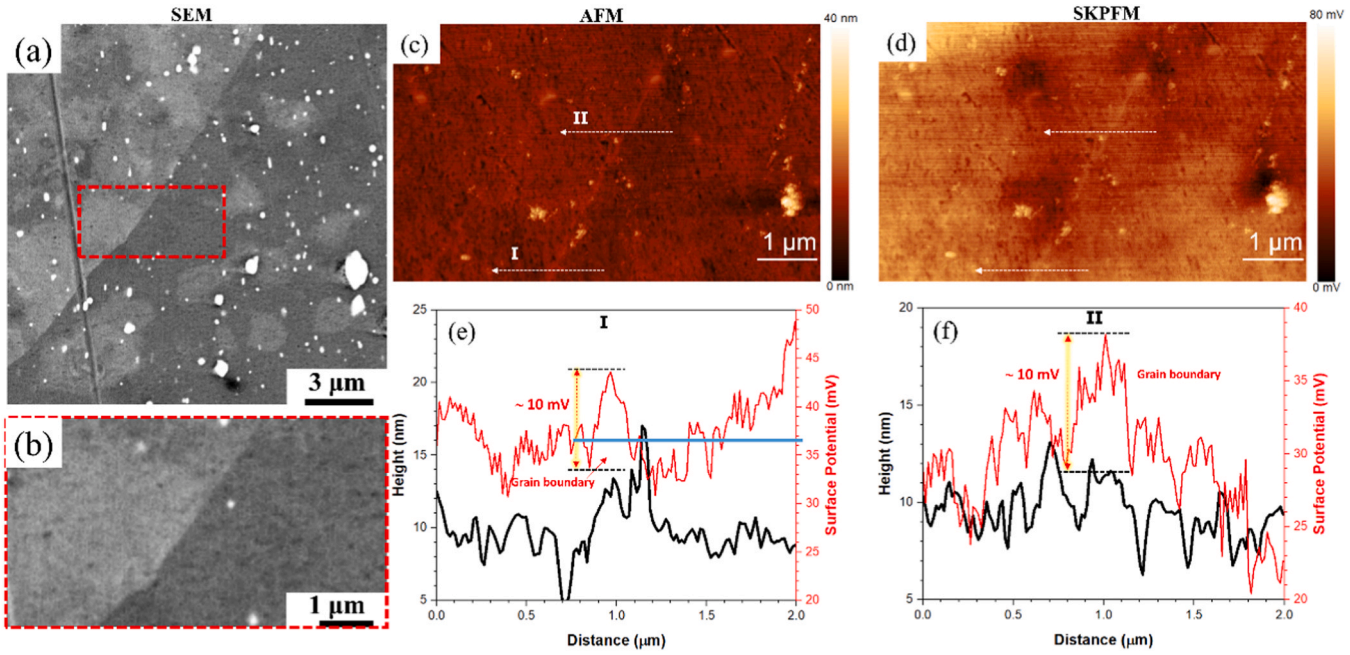

Fig. 9. (a) Low and (b) high magnification images of GB, (c) topography and (d) surface potential maps of GB in alloy R4. (e and f) Topography and surface potential line profiles in (c) and (d).

analysis alongside energy diagrams between the GB and AFM tip apex is provided (Fig. 10) to better visualize the impact of Zn-enriched precipitates located along the grain boundary (Fig. 6) on enhancing the total surface potential and/or surface charge difference. It should be emphasized that the surface potential map of grain boundaries detected by SKPFM in this study are electrical grain boundaries with a space charge region (surface potential/surface charge) instead of crystallographic grain boundaries since the AFM tip-apex is bigger than the real GB [45]. Hence, because of the localized charges at grain boundaries as defect states, a band bending occurs, resulting in changing the work function value. In the case of sample R1, the band bending is slightly downward (the rectangle-colored region in Fig. 10) with a lower "contact potential difference" (ΔCPD) which confirms less driving force for galvanic coupling at the GB and lowers the depletion of the electrons in grain boundary surrounding [46,47]. The Zn-enriched particles at grain boundaries of sample R4 triggers a more downward band bending or higher ΔCPD which confirms both greater driving force for intergranular corrosion attacks at GB and the depletion of the electrons in GB region.

5. Conclusions

In the current work, the influence of minor additions of Zn in extruded 6082 Al-Mg-Si alloys on the precipitate crystal structure and IGC in extruded 6082 Al-Mg-Si alloys has been investigated. The following conclusions are drawn from the current work:

1. A minor addition of Zn (0.06 wt%) significantly affects the IGC resistance of 6082 Al-Mg-Si alloys in the peakaged condition, as extended attacks are observed across the surface. However, the

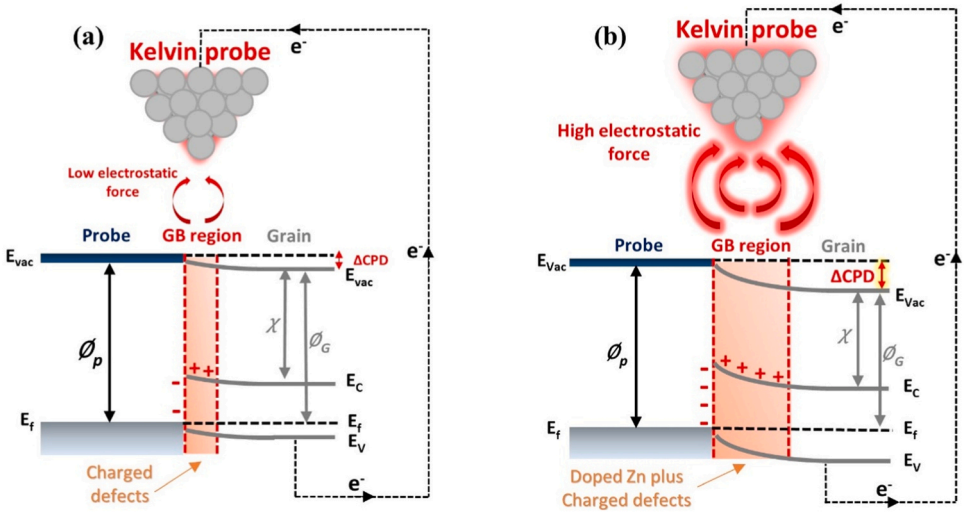

Fig. 10. Schematic demonstration of the SKPFM principle along with the energy level diagram during the electrostatic interaction between a conductive AFM tip-apex and GB without (a) and with (b) Zn enriched particles. The abbreviations defined as valence and conduction bands (E_V and E_C), Fermi level (E_f), electron affinity (χ), and vacuum level (E_{Vac}), work function of probe and grain ($\varnothing_p$ *and* $\varnothing_G$).

penetration depth increased from 37 μm in sample R1 to 137 μm in sample R4 with the highest Zn addition.
2. More elongated and larger grain boundary particles were observed in sample R4 compared to sample R1. However, despite these morphological differences, no significant variation in the width of the PFZs was observed.
3. In sample R4, a higher surface potential difference (~10 mV) was measured at the grain boundaries compared to its adjacent matrix. This suggests that the adjacent matrix will act as a cathode relative to the PFZ and GB particles.
4. The primary hardening precipitates observed in this work are β″ type, and no Mg-Zn η-type of precipitates were found.
5. Low Zn concentrations can promote the formation of Q'/C phase substructures in the hardening precipitates, which are normally found in Al-Mg-Si (-Cu) alloys. This indicates that Zn can have a similar role as Cu inside these crystal structures.
6. Zn partially occupies Si_1, Si_2, and Si_3/Al columns in pure β″, but does not occupy the Mg_1/Al, Mg_2, and Mg_3 sites.

CRediT authorship contribution statement

Emad H. Bartawi: Writing – review & editing, Writing – original draft, Methodology, Investigation, Formal analysis, Conceptualization. **Ghada Shaban:** Writing – review & editing, Investigation, Formal analysis. **Calin D. Marioara:** Writing – review & editing, Investigation, Formal analysis. **Ehsan Rahimi:** Writing – review & editing, Formal analysis. **Ruben Bjørge:** Investigation. **Jonas K. Sunde:** Writing – review & editing. **Yaiza Gonzalez-Garcia:** Writing – review & editing. **Randi Holmestad:** Writing – review & editing. **Rajan Ambat:** Writing – review & editing, Supervision, Funding acquisition, Conceptualization.

Declaration of Competing Interest

The authors declare the following financial interests/personal relationships which may be considered as potential competing interests: Emad Hasan Bartawi reports financial support was provided by Technical University of Denmark Department of Civil and Mechanical Engineering. Emad Hasan Bartawi reports a relationship with Technical University of Denmark Department of Civil and Mechanical Engineering that includes: employment. If there are other authors, they declare that they have no known competing financial interests or personal relationships that could have appeared to influence the work reported in this paper.

Acknowledgements

The authors would like to acknowledge Hydro Aluminium, Norway, for providing material. The authors also thank Dr. Ruben Bjørge from SINTEF Industry and Dr. J. Kling from DTU Nanolab for his technical assistance during STEM experiments. Emad H. Bartawi and Rajan Ambat acknowledge funding from the Independent Research Fund Denmark (grant number 9041-00240A). Also, this project has received funding from the European Union's Horizon 2020 research and innovation programme under grant agreement No 823717 – ESTEEM3. The HAADF-STEM work was done at the NORTEM infrastructure (NFR: 197405) infrastructure in Trondheim, Norway.

Data availability

Data will be made available on request.

References

[1] A.C. Serrenho, J.B. Norman, J.M. Allwood, The impact of reducing car weight on global emissions: the future fleet in Great Britain, Philos. Trans. R. Soc. A Math. Phys. Eng. Sci. 375 (2017) 20160364.
[2] D.J. Chakrabarti, D.E. Laughlin, Phase relations and precipitation in Al–Mg–Si alloys with Cu additions, Prog. Mater. Sci. 49 (2004) 389–410.
[3] J. Hirsch, Recent development in aluminium for automotive applications, Trans. Nonferrous Met. Soc. China 24 (2014) 1995–2002.
[4] W.S. Miller, L. Zhuang, J. Bottema, A.J. Wittebrood, P. De Smet, A. Haszler, A. Vieregge, Recent development in aluminium alloys for the automotive industry, Mater. Sci. Eng. A. 280 (2000) 37–49.
[5] J.R. Davis, Corrosion of aluminum and aluminum alloys, ASM international, 1999.
[6] D.V. Wilson, Aluminium versus steel in the family car — the formability factor, J. Mech. Work. Technol. 16 (1988) 257–277.
[7] V.M. Simões, M.C. Oliveira, H. Laurent, L.F. Menezes, The punch speed influence on warm forming and springback of two Al-Mg-Si alloys, J. Manuf. Process. 38 (2019) 266–278.
[8] R. Abi-Akl, D. Mohr, Paint-bake effect on the plasticity and fracture of pre-strained aluminum 6451 sheets, Int. J. Mech. Sci. (2017) 124–125, 68–82.
[9] H. Zhong, P.A. Rometsch, L. Cao, Y. Estrin, The influence of Mg/Si ratio and Cu content on the stretch formability of 6xxx aluminium alloys, Mater. Sci. Eng. A. 651 (2016) 688–697.
[10] S.K. Kairy, P.A. Rometsch, C.H.J. Davies, N. Birbilis, On the intergranular corrosion and hardness evolution of 6xxx series Al alloys as a function of Si:Mg ratio, Cu Content, and aging condition, Corrosion 73 (2017) 1280–1295.
[11] Y. Zou, Q. Liu, Z. Jia, Y. Xing, L. Ding, X. Wang, The intergranular corrosion behavior of 6000-series alloys with different Mg/Si and Cu content, Appl. Surf. Sci. 405 (2017) 489–496.
[12] A. Shi, B.A. Shaw, E. Sikora, The role of grain boundary regions in the localized corrosion of a copper-free 6111-like aluminum alloy, Corrosion 61 (2005) 534–547.
[13] E.H. Bartawi, C.D. Marioara, G. Shaban, E. Rahimi, O.V. Mishin, J.K. Sunde, Y. Gonzalez-Garcia, R. Holmestad, R. Ambat, Effects of grain boundary chemistry and precipitate structure on intergranular corrosion in Al-Mg-Si alloys doped with Cu and Zn, Corros. Sci. 236 (2024) 112227.
[14] E.H. Bartawi, O.V. Mishin, G. Shaban, F. Grumsen, J.H. Nordlien, R. Ambat, The effect of trace level copper content on intergranular corrosion of extruded AA6082-T6 alloys, Mater. Chem. Phys. (2023) 128303.
[15] A.K. Bhattamishra, K. Lal, Microstructural studies on the effect of Si and Cr on the intergranular corrosion in Al-Mg-Si alloys, Mater. Des. 18 (1997) 25–28.
[16] M.H. Larsen, J.C. Walmsley, O. Lunder, R.H. Mathiesen, K. Nisancioglu, Intergranular corrosion of copper-containing AA6xxx AlMgSi aluminum alloys, J. Electrochem. Soc. 155 (2008) C550.
[17] F. Eckermann, T. Suter, P.J. Uggowitzer, A. Afseth, P. Schmutz, The influence of MgSi particle reactivity and dissolution processes on corrosion in Al–Mg–Si alloys, Electrochim. Acta 54 (2008) 844–855.
[18] W. Yang, S. Ji, Z. Li, M. Wang, Grain boundary precipitation induced by grain crystallographic misorientations in an extruded Al-Mg-Si-Cu alloy, J. Alloy. Compd. 624 (2015) 27–30.
[19] T. Minoda, H. Yoshida, Effect of grain boundary characteristics on intergranular corrosion resistance of 6061 aluminum alloy extrusion, Metall. Mater. Trans. A. 33 (2002) 2891–2898.
[20] S.K. Kairy, T. Alam, P.A. Rometsch, C.H.J. Davies, R. Banerjee, N. Birbilis, Understanding the origins of intergranular corrosion in copper-containing Al-Mg-Si alloys, Metall. Mater. Trans. A Phys. Metall. Mater. Sci. 47 (2016) 985–989.
[21] M. de Haas, S.M. van Scherpenzeel, J.T.M. de Hosson, Grain boundary segregation and precipitation in aluminium alloy AA6061, Mater. Sci. Forum (2006) 519–521, 467–472.
[22] F.L. Zeng, Z.L. Wei, J.F. Li, C.X. Li, X. Tan, Z. Zhang, Z.Q. Zheng, Corrosion mechanism associated with Mg2Si and Si particles in Al–Mg–Si alloys, Trans. Nonferrous Met. Soc. China 21 (2011) 2559–2567.
[23] M.X. Guo, G. Sha, L.Y. Cao, W.Q. Liu, J.S. Zhang, L.Z. Zhuang, Enhanced bake-hardening response of an Al–Mg–Si–Cu alloy with Zn addition, Mater. Chem. Phys. 162 (2015) 15–19.
[24] Y.H. Cai, C. Wang, J.S. Zhang, Microstructural characteristics and aging response of Zn-containing Al-Mg-Si-Cu alloy, Int. J. Miner. Metall. Mater. 20 (2013) 659–664.
[25] M.X. Guo, Y. Zhang, X.K. Zhang, J.S. Zhang, L.Z. Zhuang, Non-isothermal precipitation behaviors of Al-Mg-Si-Cu alloys with different Zn contents, Mater. Sci. Eng. A. 669 (2016) 20–32.
[26] S. Zhu, Z. Li, L. Yan, X. Li, S. Huang, H. Yan, Y. Zhang, B. Xiong, Natural aging behavior in pre-aged Al–Mg–Si–Cu alloys with and without Zn addition, J. Alloy. Compd. 773 (2019) 496–502.
[27] M.X. Guo, Y.D. Zhang, G.J. Li, S.B. Jin, G. Sha, J.S. Zhang, L.Z. Zhuang, E. J. Lavernia, Solute clustering in Al-Mg-Si-Cu-(Zn) alloys during aging, J. Alloy. Compd. 774 (2019) 347–363.
[28] X.P. Ding, H. Cui, J.X. Zhang, H.X. Li, M.X. Guo, Z. Lin, L.Z. Zhuang, J.S. Zhang, The effect of Zn on the age hardening response in an Al-Mg-Si alloy, Mater. Des. 65 (2015) 1229–1235.
[29] T. Saito, S. Wenner, E. Osmundsen, C.D. Marioara, S.J. Andersen, J. Røyset, W. Lefebvre, R. Holmestad, The effect of Zn on precipitation in Al-Mg-Si alloys, Philos. Mag. 94 (2014) 2410–2425.
[30] S. Zhu, Z. Li, L. Yan, X. Li, S. Huang, H. Yan, Y. Zhang, B. Xiong, Effects of Zn addition on the age hardening behavior and precipitation evolution of an Al-Mg-Si-Cu alloy, Mater. Charact. 145 (2018) 258–267.
[31] L. Li, S. Ji, Q. Zhu, Y. Wang, X. Dong, W. Yang, S. Midson, Y. Kang, Effect of Zn concentration on the microstructure and mechanical properties of Al-Mg-Si-Zn alloys processed by gravity die casting, Metall. Mater. Trans. A. 49 (2018) 3247–3256.

[32] S.J. Andersen, C.D. Marioara, J. Friis, R. Bjørge, Q. Du, I.G. Ringdalen, S. Wenner, E.A. Mørtsell, R. Holmestad, T. Saito, J. Røyset, O. Reiso, Directionality and column arrangement principles of precipitates in Al-Mg-Si-(Cu) and Al-Mg-Cu linked to line defect in Al, Mater. Sci. Forum 877 (2017) 461–470.
[33] T. Saito, E.A. Mørtsell, S. Wenner, C.D. Marioara, S.J. Andersen, J. Friis, K. Matsuda, R. Holmestad, Atomic structures of precipitates in Al–Mg–Si alloys with small additions of other elements, Adv. Eng. Mater. 20 (2018) 1800125.
[34] S.J. Andersen, H.W. Zandbergen, J. Jansen, C. Træholt, U. Tundal, O. Reiso, The crystal structure of the β″ phase in Al-Mg-Si Alloys, Acta Mater. 46 (1998) 3283–3298.
[35] E.H. Bartawi, C.D. Marioara, G. Shaban, C. Hatzoglou, R. Holmestad, R. Ambat, Atomic Structure of Hardening Precipitates in Al-Mg-Si Alloys: influence of Minor Additions of Cu and Zn, ACS Nano 17 (2023) 24115–24129, https://doi.org/10.1021/acsnano.3c09129.
[36] Z. Esfahani, E. Rahimi, M. Sarvghad, A. Rafsanjani-Abbasi, A. Davoodi, Correlation between the histogram and power spectral density analysis of AFM and SKPFM images in an AA7023/AA5083 FSW joint, J. Alloy. Compd. 744 (2018) 174–181.
[37] C. Örnek, C. Leygraf, J. Pan, On the Volta potential measured by SKPFM–fundamental and practical aspects with relevance to corrosion science, Corros. Eng. Sci. Technol. 54 (2019) 185–198.
[38] Y. Birol, Effect of Cr and Zr on the grain structure of extruded en AW 6082 alloy, Met. Mater. Int. 20 (2014) 727–732.
[39] Y. Mahmoodkhani, J. Chen, M.A. Wells, W.J. Poole, N.C. Parson, The effect of die bearing geometry on surface recrystallization during extrusion of an Al-Mg-Si-Mn alloy, Metall. Mater. Trans. A Phys. Metall. Mater. Sci. 50 (2019) 5324–5335.
[40] P.K. Saha, Aluminum Extrusion Technology, ASM International, 2000.
[41] K.M. Fleming, A. Zhu, J.R. Scully, Corrosion of AA6061 brazed with an Al-Si alloy: effects of Si on metallurgical and corrosion behavior, Corrosion 68 (2012) 1126–1145.
[42] E.H. Bartawi, O.V. Mishin, G. Shaban, J.H. Nordlien, R. Ambat, Electron microscopy analysis of grain boundaries and intergranular corrosion in aged Al-Mg-Si alloy doped with 0.05 wt% Cu, Corros. Sci. 209 (2022) 110758.
[43] L. Nguyen, T. Hashimoto, D.N. Zakharov, E.A. Stach, A.P. Rooney, B. Berkels, G. E. Thompson, S.J. Haigh, T.L. Burnett, Atomic-scale insights into the oxidation of aluminum, ACS Appl. Mater. Interfaces 10 (2018) 2230–2235.
[44] E. Rahimi, A. Imani, M. Lekka, F. Andreatta, Y. Gonzalez-Garcia, J.M.C. Mol, E. Asselin, L. Fedrizzi, Morphological and surface potential characterization of protein nanobiofilm formation on magnesium alloy oxide: their role in biodegradation, Langmuir 38 (2022) 10854–10866.
[45] J. Gonzalez-Julian, K. Neuhaus, M. Bernemann, J. Pereira da Silva, A. Laptev, M. Bram, O. Guillon, Unveiling the mechanisms of cold sintering of ZnO at 250 °C by varying applied stress and characterizing grain boundaries by Kelvin probe force microscopy, Acta Mater. 144 (2018) 116–128.
[46] T. Glatzel, S. Sadewasser, R. Shikler, Y. Rosenwaks, M.C. Lux-Steiner, Kelvin probe force microscopy on III–V semiconductors: the effect of surface defects on the local work function, Mater. Sci. Eng. B. 102 (2003) 138–142.
[47] C. Leendertz, F. Streicher, M.C. Lux-Steiner, S. Sadewasser, Evaluation of Kelvin probe force microscopy for imaging grain boundaries in chalcopyrite thin films, Appl. Phys. Lett. 89 (2006).